Research Square

Preprints are preliminary reports that have not undergone peer review.
They should not be considered conclusive, used to inform clinical practice,
or referenced by the media as validated information.

Functional neuroimaging identifies a cross-species biomarker for treatment monitoring in Angelman syndrome

Laura Baroncelli

baroncelli@in.cnr.it

Neuroscience Institute https://orcid.org/0000-0001-6739-2860

Lorenzo Dadà

Scuola Normale Superiore

Camilla Simoncelli

IRCCS Stella Maris Foundation, Pisa, Italy

Giulia Sagona

Fondazione Stella Maris

Giacomo Vecchieschi

IRCCS Stella Maris Foundation

Chiara De Cesari

Consiglio Nazionale delle Ricerche (CNR) https://orcid.org/0009-0004-2305-966X

Rebecca Diversi

Neuroscience Institute

Francesca Biondi

Neuroscience Institute

Paymaan Jafar-nejad

Ionis Pharmaceuticals

Chiara Bosetti

IRCCS Stella Maris Foundation

Giulia Prisco

Organizzazione Sindrome di Angelman Onlus

Raffaele Mazziotti

University of Florence https://orcid.org/0000-0001-5344-5079

Ilaria Tonazzini

Consiglio Nazionale delle Ricerche (CNR) https://orcid.org/0000-0002-7323-2174

Roberta Battini

IRCCS Fondazione Stella Maris https://orcid.org/0000-0002-7889-1355

Article

Keywords:

Posted Date: July 31st, 2026

DOI: https://doi.org/10.21203/rs.3.rs-9937060/v1

License: This work is licensed under a Creative Commons Attribution 4.0 International License.
Read Full License

Additional Declarations: There is **NO** Competing Interest.

Functional neuroimaging identifies a cross-species biomarker for treatment monitoring in Angelman syndrome

Authors: Lorenzo Dadà[1,2*], Camilla Simoncelli[3*], Giulia Sagona[4], Giacomo Vecchieschi[3,5], Chiara De Cesari[6], Rebecca Diversi[4], Francesca Biondi[4], Paymaan Jafar-Nejad[7], Chiara Bosetti[3], Giulia Prisco[8], Raffaele M. Mazziotti[4,9], Ilaria Tonazzini[6], Roberta Battini[3,10], Laura Baroncelli[3,4]

1. BIO@SNS Lab, Scuola Normale Superiore di Pisa, Pisa 56126, Italy
2. Department of Statistics, Computer Science, Applications "Giuseppe Parenti" (DiSIA), University of Florence, Florence 50134, Italy
3. Department of Developmental Neuroscience, IRCCS Stella Maris Foundation, Pisa 56128, Italy
4. Institute of Neuroscience, National Research Council (CNR), 56127 Pisa, Italy
5. Department of Translational Research and New Technologies in Medicine and Surgery, University of Pisa, Pisa 56126, Italy
6. Nanoscience Institute, National Research Council (CNR), NEST-SNS, 56127 Pisa, Italy
7. Ionis Pharmaceuticals, Carlsbad, CA, 92010, USA
8. OR.S.A, Organizzazione Sindrome di Angelman Onlus, Italy
9. Department of NEUROFARBA, University of Florence, 50139 Florence, Italy
10. Department of Clinical and Experimental Medicine, University of Pisa, 56126 Pisa, Italy

*These authors contributed equally to this work

Corresponding Author:
Laura Baroncelli, PhD
Neuroscience Institute CNR
Via Giuseppe Moruzzi 1, 56124, Pisa, Italy
laura.baroncelli@cnr.it
Tel. +39 0503153199

Abstract

Angelman syndrome (AS) is a neurodevelopmental disorder for which non-invasive biomarkers suitable for longitudinal monitoring and clinical trials remain limited. Although EEG abnormalities have shown promise as treatment-responsive biomarkers, their applicability may be constrained by tolerability and developmental variability. Here, we identify visually evoked hemodynamic responses as a robust cross-species functional biomarker of AS. Using intrinsic optical signal (IOS) imaging, we show that AS mouse model exhibits enhanced visual cortical responses that persist across development and partially reflect disease severity in adulthood. These alterations are highly sensitive to therapeutic interventions: restoration of UBE3A expression normalizes visual responses and scales with both behavioral recovery and molecular rescue. To assess translational relevance, we performed functional near-infrared spectroscopy (fNIRS) in individuals with AS during visual stimulation, demonstrating the feasibility of fNIRS in behaviorally challenging settings. Individuals with AS display amplified and temporally altered hemodynamic responses that are consistently detected across preprocessing strategies and remaine stable across age. Our findings demonstrate that visually evoked hemodynamic responses capture a disease-specific cortical signature of AS conserved across species. The scalability, non-invasiveness, and feasibility of fNIRS, combined with preclinical sensitivity to therapeutic interventions, position neurovascular imaging as a promising biomarker for future clinical trials in AS.

Introduction

Angelman syndrome (AS) is a rare neurodevelopmental disorder characterized by severe intellectual disability, motor dysfunction, absence of speech, seizures, and behavioral abnormalities[1]. The disorder is caused by disruption of the maternally inherited *UBE3A* gene. In neurons, the paternal *UBE3A* allele is epigenetically silenced by the expression of a long non-coding antisense RNA (*UBE3A-ATS*), leaving the maternal gene as the sole source of UBE3A protein expression[2]. Consequently, genetic alterations affecting the maternal allele, including deletions or mutations, paternal uniparental disomy, or imprinting defects, result in neuronal loss of UBE3A and lead to the development of AS[3].

Currently, no disease-modifying therapies are available for AS, and clinical management remains largely symptomatic[4]. Over the past decade, several therapeutic strategies have been explored in AS mouse models, including antisense oligonucleotides (ASOs), gene transfer therapy, and small-molecule approaches[5–13]. Notably, both gene transfer therapy and ASO-based therapies targeting *UBE3A-ATS* to unsilence the paternal allele have recently entered clinical trials[6,14] (e.g., ClinicalTrials.gov identifiers: NCT06914609; NCT07136454; NCT07157254; NCT07181837), underscoring the urgent need for reliable and quantitative outcome measures to monitor disease progression and assess therapeutic efficacy.

Electroencephalography (EEG)-based metrics have emerged from previous studies as promising functional biomarkers for AS. In particular, abnormally elevated delta-band rhythmicity has been consistently reported in both AS mouse models and patients[15,16]. However, longitudinal EEG recordings in humans indicate that delta power progressively decreases with age, suggesting that this biomarker might be most sensitive during early development and less reliable in older individuals. In addition, EEG recordings are often poorly tolerated by children with AS, limiting their feasibility in clinical settings and longitudinal studies[17]. Together, these limitations highlight the need for alternative biomarkers that can be robustly applied across the lifespan.

Here, we investigated highly translational optical imaging approaches, Intrinsic Optical Signal (IOS) imaging in mice and functional Near-Infrared Spectroscopy (fNIRS) in humans, to assess visually evoked responses as functional brain readouts in AS. Both neuroimaging techniques measure activity-dependent hemodynamic changes and provide non-invasive measures of cortical function that are complementary to electrophysiological recordings. The visual system represents a particularly suitable model for probing cortical dysfunction in neurodevelopmental disorders[18–21]. Sensory processing alterations in the visual domain have been reported in AS, and neuroimaging studies in patients have identified structural abnormalities in the occipital cortex, including reduced grey matter volume and cortical thickness[22]. Consistently, maternal loss of *Ube3a* in mice disrupts synaptic plasticity in the visual cortex, impairing experience-dependent circuit maturation[23,24].

Building on this evidence, we evaluated visually evoked hemodynamic responses as a candidate prognostic and treatment-responsive biomarker for AS. In the mouse model, we observed significantly enhanced visual responses in AS animals compared to wild-type (WT) controls. These alterations partially correlated with the severity of motor deficits. Importantly, visual responses were sensitive to therapeutic interventions: reinstatement of UBE3A expression through either gene transfer therapy or ASO treatment normalized visual responses in AS mice, and the extent of recovery correlated with both motor improvement and cortical UBE3A levels. Strikingly, a similar pattern of enhanced visually evoked responses was also observed in individuals with AS, where cortical activity was assessed using fNIRS, supporting the translational relevance of this measure across species.

Collectively, our findings demonstrate that visually evoked hemodynamic responses measured using non-invasive optical imaging techniques represent a sensitive, quantitative, and cross-species functional biomarker for monitoring disease progression and therapeutic efficacy in AS.

Results

Enhanced visually evoked cortical responses persist across development in AS mice

To evaluate whether visual cortical hemodynamic responses could serve as a functional biomarker of brain dysfunction in AS, we first characterized visually evoked cortical activity using IOS imaging in juvenile (postnatal day 45, P45) AS mice and their WT littermate controls. As shown in Fig. 1b, contralateral eye stimulation elicited the canonical IOS response pattern in both genotypes. However, quantitative analysis revealed that the amplitude of visually evoked responses was significantly increased in AS mice compared to WT controls (Fig. 1c). This alteration was comparable in male and female animals, indicating that the abnormal visual response amplitude was not sex-dependent (Fig. 1d).

To determine whether these alterations persist beyond early developmental stages, visually evoked IOS responses were recorded in an independent cohort of adult mice at P90. Adult AS mice displayed a response profile similar to that observed at P45, with significantly higher IOS amplitudes compared to WT animals in both sexes (Fig. 1e, f). Together, these findings indicate that abnormal visually evoked hemodynamic responses are a stable and persistent feature of the AS mouse model, supporting the robustness of visual IOS measures as a readout of cortical processing across development.

Visual cortical hemodynamic hyper-responsiveness partially reflects motor impairment in adult AS mice

To determine whether altered visual cortical responses are associated with disease severity, we examined the relationship between IOS response amplitude and behavioral performance in juvenile and adult mice[25]. At both P45 and P90, AS mice exhibited the expected behavioral impairments compared to WT littermates, including deficits in motor coordination in the rotarod test, reduced digging behavior in the marble burying assay, and decreased locomotory activity in the open field[25] (Supplementary Fig. 1).

In adult P90 AS mice, IOS response amplitude was inversely correlated with rotarod performance, indicating that animals with greater visual cortical hyper-responsiveness tended to exhibit poorer motor coordination (Fig. 2a). A similar trend was observed for marble burying performance, although this association did not reach statistical significance (Fig. 2b). No relationship was detected with open-field locomotor activity (Fig. 2c). In contrast, no significant correlations between IOS measures and behavioral performance were observed in juvenile AS mice (Supplementary Fig. 2). Together, these findings suggest that altered visual cortical responses capture specific aspects of disease severity in adult AS mice. Although IOS measures do not broadly predict behavioral dysfunction across all domains, their association with motor performance supports the biological relevance of this imaging readout and indicates that it reflects functionally meaningful features of the AS phenotype.

Random forest can be a robust and sensitive diagnostic classifier

To evaluate whether IOS imaging features alone, or in combination with behavioral measures, could reliably discriminate genotypes, we applied a Random Forest classifier, a machine learning approach well suited to integrate multiple variables and identify the features that best

contribute to classification performance (Supplementary Figure 3). The classifier trained on combined IOS and behavioral features showed strong performance in distinguishing WT and AS mice (n = 67). Ten-fold cross-validation confirmed robust generalization, with accuracy ranging from 0.84 to 0.90, alongside consistently high precision, recall, and F1-score, and low variability across folds. The model achieved an AUC of 0.97, with low false positive (0.11) and false negative (0.12) rates, indicating excellent discriminative power. Statistical significance was assessed using a permutation test in which class labels were randomly shuffled (n = 1000 iterations). The observed cross-validated accuracy (0.85) was markedly higher than chance, as indicated by the permutation distribution (mean = 0.5, SD = 0.07) and a significant permutation test (p = 0.001). These results confirm that model performance captures meaningful structure in the data rather than random variation.

Moreover, feature importance analysis revealed that, while behavioral variables ranked among the strongest predictors, IOS-derived measures, including peak amplitude and average response amplitude, made a substantial and independent contribution to classification accuracy, supporting a complementary role of neurophysiological features in group discrimination. Detailed results are reported in Supplementary Table 2.

This underscores the central role of imaging-based features as objective and quantitative markers that significantly enhance model performance while providing biologically meaningful discrimination between groups. Importantly, IOS-derived measures contribute complementary and non-redundant information to behavioral readouts, strengthening the overall classification framework.

Visual IOS responses are a sensitive readout of therapeutic efficacy in the AS mouse model

To further assess the translational relevance of visually evoked IOS responses, we examined their sensitivity to therapeutic interventions previously shown to restore UBE3A protein expression in the AS brain, including gene transfer therapy and early ASO administration[5,6,11,26,27] (Fig. 3a, h). IOS recordings were performed at developmental time points previously identified as showing robust therapeutic effects for each treatment paradigm[5,6].

We found that perinatal gene transfer therapy fully normalized visually evoked IOS responses in AS mice at both juvenile and adult stages (Fig. 3b, c). Consistent with these findings, treated animals showed a significant improvement in motor coordination, with rotarod performance comparable to WT mice (Fig. 3d). Western blot analysis confirmed robust restoration of cortical UBE3A protein levels in AAV-treated AS mice, reaching over 70% of WT expression (Fig. 3f, Supplementary Fig. 4a). Importantly, IOS amplitude significantly correlated with both rotarod performance and cortical UBE3A levels (Fig. 3e, g), indicating that visual IOS measures provide a quantitative and biologically meaningful readout of therapy-induced recovery.

Similarly, administration of ASO at P1 rescued visually evoked IOS responses in AS mice at P35 (Fig. 3i) and significantly increased UBE3A expression levels compared to phosphate-buffered saline (PBS)-injected AS mice (Fig. 3l, Supplementary Fig. 4b), further demonstrating that visual cortical alterations are reversible and treatment-sensitive. Notably, IOS amplitude showed a trend toward correlation with UBE3A expression levels in ASO-treated mice, although this association did not reach statistical significance (Fig. 3m).

Collectively, our findings establish visually evoked IOS responses as a sensitive, robust, and treatment-responsive functional imaging biomarker of cortical dysfunction in AS. This

readout not only captures disease-specific alterations and reflects phenotypic severity in adulthood, but also reliably tracks therapeutic efficacy across distinct intervention strategies.

fNIRS reveals altered hemodynamic signatures in AS individuals

To evaluate the translational potential of hemodynamic responses as a functional biomarker in AS, we performed functional near-infrared spectroscopy (fNIRS) during visual stimulation in individuals with AS and neurotypical controls. The study included 59 individuals with AS (age range: 2–40 years) carrying different AS genotypes, and 45 neurotypical controls (age range: 2–48 years) (see Supplementary Table 3 for detailed demographics and genotypic information). The portability of fNIRS enabled an itinerant data collection strategy across multiple regions in Italy, implemented during events organized by the Italian AS-parent association Organizzazione Sindrome di Angelman (OR.S.A.). Within this framework, we obtained data of sufficient quality in 83% of AS participants (N= 49), supporting the feasibility of this approach in real-world settings.

Because recordings were performed in a behaviorally challenging population particularly prone to movement during acquisition, we initially analyzed the data using a previously validated standard preprocessing pipeline[28,29] and subsequently implemented a more stringent approach specifically optimized for motion-artifact correction. Importantly, the main abnormalities observed in AS were consistently detected across both approaches, supporting the reproducibility of the findings. Indeed, stimulus-evoked hemodynamic responses were consistently detected in both AS participants and controls. Visual stimulation elicited increases in oxygenated hemoglobin (HbO) and total hemoglobin (HbT), together with a concomitant decrease in deoxygenated hemoglobin (HbR) relative to baseline, whereas no such changes were observed in the mock condition (Fig. 4,5). These findings establish that fNIRS can reliably capture cortical responses in individuals with AS.

Importantly, individuals with AS exhibited a distinct and consistently altered hemodynamic profile. Compared to controls, HbO and HbR responses were characterized by greater amplitude, broader temporal dynamics, and increased variability, indicating altered neurovascular dynamics following visual stimulation (Fig. 4,5).

The second, enhanced preprocessing pipeline produced cleaner signals with closer correspondence to the canonical hemodynamic response function (Supplementary Fig. 5a) and enabled the identification of additional abnormalities in AS response dynamics, including prolonged time-to-peak responses (Supplementary Fig. 5b), which were less evident using the standard preprocessing approach (Supplementary Fig. 6).

Leveraging this improved signal fidelity, we next examined age-related effects. In neurotypical controls, HbO and HbT amplitudes showed the expected age-related attenuation, with an opposite trend for HbR (Supplementary Fig. 7a-b, 8a-b), consistent with previous literature[28,30–32]. A comparable developmental profile was also observed in AS individuals when using the enhanced preprocessing pipeline (Supplementary Fig. 8). Importantly, despite these shared developmental trends, the increased response amplitude in AS persisted across age. After normalization for age-predicted control responses, HbO values in the AS group remained significantly elevated, and directional tests of the excess-response slope showed neither increase nor decrease with age (Supplementary Fig. 8c), indicating that this enhanced hemodynamic response represents a stable, disease-specific feature.

Together, these findings establish fNIRS as a robust and scalable translational biomarker of cortical dysfunction in AS, directly bridging preclinical and human studies and supporting its use as an objective outcome measure in clinical trials.

Discussion

Angelman syndrome is a severe neurodevelopmental disorder characterized by profound cognitive and motor impairments, for which the development of reliable biomarkers remains a critical unmet need. In this context, the visual system has emerged as a powerful model to probe cortical dysfunction in neurodevelopmental disorders, providing quantitative and translational readouts across species. Previous studies have demonstrated that visual evoked potentials (VEPs) capture neural alterations in both animal models and patients with Rett syndrome and CDKL5 deficiency disorder[18–20], while emerging evidence indicates that visual neurovascular coupling can serve as a sensitive marker of cortical processing in CDKL5 deficiency[20] and Creatine Transporter Deficiency[21].

Here, we show that visually evoked hemodynamic activity is markedly altered in AS mice. Increased IOS responses were consistently observed across developmental stages, indicating that this phenotype is stable over time and supporting its use as a biomarker in AS. Although AS is primarily characterized by severe motor impairments, we focused on the visual cortex because visually evoked IOS responses provide a robust and highly translational measure of cortical function. Unlike motor cortex recordings, which require stereotyped motor behaviors that are difficult to standardize, visual stimulation can be precisely controlled in both mice and humans, enabling direct cross-species comparisons. The absence of sex-dependent differences further suggests that these alterations represent a core genotype-driven feature[25,33,34]. Importantly, rather than reflecting a simple increase in activation, our data indicate a qualitatively distinct neurovascular state in AS, pointing to fundamental alterations in cortical processing.

At the mechanistic level, these abnormalities likely arise from the convergence of metabolic and circuit-level dysfunctions. IOS signals reflect activity-dependent changes in metabolic demand and neurovascular coupling, suggesting that alterations in cellular metabolism may directly contribute to the observed phenotype. Extensive evidence in AS models demonstrates widespread impairments in cellular energy metabolism, particularly within the hippocampus. These include increased levels of reactive oxygen species (ROS) in CA1 pyramidal neurons, associated with impaired long-term potentiation (LTP) and memory deficits[35], as well as abnormal mitochondrial morphology, reduced oxidative phosphorylation complex III activity[36], and defects in autophagy and protein metabolism[37]. Our findings extend these metabolic alterations beyond the hippocampus to cortical regions, including the visual cortex, indicating that disrupted metabolic support may broadly impair neurovascular coupling. Notably, mitochondrial dysfunction and oxidative stress have also been reported at embryonic stages in AS mouse models[38,39], raising the possibility that neurovascular deficits may emerge early during development. In parallel circuit-level abnormalities, particularly involving GABAergic interneurons and excitation–inhibition imbalance[40], are likely to further contribute to altered hemodynamic responses in AS animals. Synaptic and network dysfunctions have been reported across multiple brain regions in AS mice, including hippocampal and cortical areas[40–43]. Within the visual cortex, maternal loss of *Ube3a* impairs experience-dependent visual cortical plasticity[23,24] and disrupts processing in higher visual areas[44]. These alterations are associated with neuron-type-specific synaptic alterations that preferentially affect GABAergic interneurons, leading to an imbalance between excitation and inhibition within cortical circuits[45]. Reduced inhibitory input in cortical layer 2/3 increases the excitability of pyramidal neurons, thereby elevating activity-dependent metabolic demand during sensory stimulation. This provides a plausible mechanistic connection between circuit dysfunction and the exaggerated

hemodynamic responses observed in AS mice during IOS recordings[46,47]. Within this framework, adenosine may act as a key metabolic sensor[48] linking metabolic and synaptic dysfunctions to the observed hemodynamic alterations. Consistent with this view, dysregulation of adenosine signaling has been implicated in AS pathology. Increased density of adenosine A2A receptors has been reported in the hippocampus of AS mice, and pharmacological blockade of these receptors rescues motor deficits, synaptic alterations in cerebellar and striatal circuits, and hippocampal memory impairments[49,50]. Together, these data suggest that altered adenosine signalling may represent a mechanistic bridge between metabolic dysfunction, circuit-level alterations, and impaired neurovascular coupling in AS.

To further assess the utility of this biomarker, we examined its relationship with disease severity and its responsiveness to therapeutic interventions. Correlations between visually evoked responses and behavioral impairments emerged in adult mice but were not detected at juvenile stages. Moreover, these associations were restricted to specific behavioral domains, suggesting that visually evoked responses do not provide a direct surrogate of overall behavioral performance. Rather, they appear to capture distinct aspects of circuit dysfunction that are only partially reflected by behavioral measures. This observation is consistent with the multifaceted nature of the AS phenotype, in which individual behavioral measures reflect the integrated function of multiple neural systems. In contrast, IOS imaging provides a direct and quantitative assessment of cortical function, enabling the detection of circuit-level abnormalities that may not be fully represented by any single behavioral outcome. Consistent with this interpretation, our machine-learning analysis identified imaging-derived features as major contributors to classification performance, supporting the notion that visually evoked responses capture disease-relevant information that is complementary to conventional behavioral measures.

Crucially, we also found that these imaging measures are highly sensitive to therapeutic interventions. Restoration of UBE3A expression through either gene transfer therapy or ASO-mediated paternal allele reactivation normalized visually evoked responses in transgenic mice and scaled with both behavioral recovery and molecular rescue, indicating that hemodynamic signals directly reflect treatment efficacy. The correlation between IOS normalization, motor improvement, and molecular rescue indicates that visually evoked responses capture functionally relevant aspects of brain recovery. Given the widespread reinstatement of UBE3A expression achieved by both gene transfer therapy and ASO treatment[5,6], visual cortex IOS responses reflect global cortical rescue rather than local circuit-specific effects. These properties position neurovascular imaging as a particularly suitable candidate biomarker for tracking target engagement and functional rescue in preclinical therapeutic studies at both juvenile and adult stages.

Building on these robust preclinical findings, we demonstrate that a comparable neurovascular signature can be reliably detected in AS individuals using fNIRS. Despite the substantial challenges associated with neuroimaging in this population, we obtained high-quality recordings in the majority of participants under real-world conditions, representing a marked improvement over previous reports[51]. These results strongly support the feasibility of fNIRS as a practical, scalable, and clinically applicable tool for probing cortical function in AS. Importantly, the successful implementation of an itinerant acquisition strategy further highlights the adaptability of fNIRS to decentralized and real-world clinical settings. The persistence of enhanced hemodynamic response across age indicates that this alteration represents a stable feature of AS rather than a transient developmental effect. This stability represents a critical requirement for biomarker development and qualification in clinical contexts. Our findings also

align with previous reports describing hypersensitive sensory phenotype in AS[52–55], suggesting that the amplified hemodynamic response may represent a physiological correlate of altered sensory processing and integration.

Importantly, the core disease-associated alterations were robustly detected across independent preprocessing strategies, demonstrating that the observed neurovascular phenotype is not driven by analytical choices or residual motion-related confounds. The implementation of a more stringent preprocessing pipeline increased signal fidelity and enabled the resolution of additional abnormalities in response dynamics, revealing subtle physiological alterations that were not fully captured by standard preprocessing approaches.

Together, our findings establish visually evoked hemodynamic activity as a robust, reproducible, and translationally relevant biomarker of cortical dysfunction associated with AS across both preclinical and human studies. This cross-species convergence positions neurovascular imaging as a powerful translational framework of directly bridging mechanistic studies in animal models with clinical investigations in patients. Importantly, the scalability, non-invasiveness, and demonstrated feasibility of fNIRS in real-world settings, combined with the sensitivity of analogous measures to therapeutic rescue in the AS mouse model, support its near-term applicability as an objective biomarker for clinical trials. Its practical ease of use and adaptability further strengthen its potential for longitudinal monitoring and therapeutic assessment in AS.

Material and methods

Animals

We used mice carrying a deletion of the maternal *Ube3a* gene (*Ube3a*$^{p+/m-}$)[56] on a C57BL/6J background. To maintain the colony, *Ube3a*$^{p-/m+}$ males were first crossed with WT females. Then, experimental heterozygous animals (*Ube3a*$^{p+/m-}$; hereafter referred to as AS) were generated by crossing *Ube3a*$^{p-/m+}$ females with WT males. *Ube3a*$^{p+/m+}$ WT littermates were used as control. Genotyping was performed as previously described[56]. Mice were housed in groups of 2-5 per cage under controlled environmental conditions (temperature 21±1°C, humidity 60±10%) with a 12 h light/dark cycle. Food and water were provided ad libitum. All experiments were conducted in compliance with the directive of the European Communities Council 63/2010 and approved by the Italian Ministry of Health (authorization number 582/2021-PR).

Experimental design for the mouse study

WT and AS mice underwent IOS recording at P45. Two days later, animals were subjected to a behavioral test battery including rotarod, marble burying, and open field, with one day of rest between tests. To avoid potential confounding effects of repeated behavioral testing, a separate cohort of WT and AS mice was tested starting at P90 (Fig. 1a). To assess therapeutic rescue, two additional groups of AS mice received intracerebroventricular (ICV) injections at P1 of either PHP.B/hUBE3Aopt[6] or PBS as control. These animals underwent longitudinal IOS recordings at P45 and P90. A reduced number of animals were available at P90 in the PHP.B/hUBE3Aopt group due to loss of the cranial ring, while PBS-treated animals were not recorded longitudinally. Two days after the final IOS session, mice were tested on the rotarod and subsequently sacrificed for quantification of cortical UBE3A expression.

Finally, two groups of P1 AS mice received ICV injections of either Ube3a ASO or PBS. The ASO used was selective for the murine UBE3A-ATS and was provided by Ionis Pharmaceuticals[11,27,57]. These animals underwent IOS recording at P35 and were sacrificed at P42 for tissue collection and subsequent quantification of cortical UBE3A expression.

Intrinsic optical signal imaging

Surgical preparation and IOS recordings were performed as previously described[21,58]. Briefly, mice were anaesthetized with isoflurane (1-3%), and a thin layer of cyanoacrylate was applied to the exposed skull to secure a custom-made metal ring (9 mm internal diameter) over the binocular visual cortex. IOS recordings were conducted under light isoflurane anesthesia (0.5-1%) supplemented with chlorprothixene (1.5 mg/Kg, i.p.). Images were acquired using a custom microscope (Leica Microsystem) under red light illumination (630 nm) provided by eight individually addressable LEDs (WS2812) mounted on the objective (Leica Z6 APO coupled with a Leica PanApo 2.0X 10447170) using a custom 3D-printed conical holder[59]. Mice were secured under the objective using a ring-shaped magnet integrated into an Arduino-based imaging chamber. Visual stimuli were generated using MATLAB Psychtoolbox and presented on a monitor positioned 15 cm from the mouse's eye. Sinusoidal gratings (spatial frequency 0.03 cycles/degree; mean luminance 20 cd/m^2; contrast 90%) were presented in the binocular visual field. The stimulus consisted of abrupt contrast reversals at 4 Hz. Images were acquired at 30 frames/s with a resolution of 512 x 512 pixels, and responses were averaged across at least 80 trials. Regions of interest (ROIs) were defined from the mean contralateral eye response by selecting pixels corresponding to the lowest 30% ΔR/R values within the range between maximal and minimal intensity. IOS amplitude was quantified as the mean signal intensity within the ROI. Because neuronal activation induces a decrease in reflectance, IOS amplitudes are intrinsically negative. Therefore, inverted values of the mean IOS amplitude are reported for clarity, with larger values corresponding to stronger visual responses.

Behavioral testing

To minimize circadian variability, all behavioral experiments were conducted within the same daily time window during the light phase (2-6 PM).

Rotarod- Testing consisted of three trials separated by at least 5 min. During each trial, mice were placed on the accelerating rotarod (4-40 rpm over 10 min), and the latency to fall was recorded. The average latency across trials was calculated for each animal.

Marble burying- Mice were individually placed in cages containing 5 cm of bedding material, with twenty blue glass marbles arranged in a 5x4 grid on the surface. After 30 min, animals were returned to their home cages, and the number of marbles buried by at least 50% was counted.

Open Field- The open field arena measured 60 × 60 cm, with a white floor and 30-cm-high black walls. Mice were allowed to freely explore the arena for 10 min while being tracked with EthoVision XT (Noldus). Total distance travelled was automatically quantified.

Intracerebroventricular injections

P1 mice were anesthetized on ice and placed on a cooled stereotaxic platform. Ventricular coordinates were identified using lambda as a reference point (X, Y, Z= +1, ± 0.3, -2 mm). A volume of 0.5 µL of PHP.B/hUBE3Aopt vector (1.6x10^{11} vg/mouse) or ASO (30 µg/mouse) was bilaterally injected using a glass capillary connected to a Hamilton syringe mounted on a micropump. Injections were delivered over 60 s.

Antisense oligonucleotides

All chemically modified oligonucleotides were synthesized and purified according to previously reported procedures[60]. The antisense oligonucleotides used in this study were 20-mer 2′-O-

methoxyethyl (MOE) gapmers, consisting of a central stretch of ten 2′-deoxynucleotides flanked on both the 5′ and 3′ ends by five MOE-modified nucleotides. The backbone was uniformly phosphorothioate, except at positions marked with “o” in the sequences, which denote phosphodiester linkages. The sequences were: control ASO, 5′-TCoGoCoCGAATACCAAoToGTT-3′; and Ube3a-as ASO, 5′-CCoAoGoCoCTTGTTGGATAoToCAT-3′. Lyophilized ASOs were reconstituted in phosphate-buffered saline (PBS) without Ca^{2+} or Mg^{2+} (Gibco, cat. no. 14190).

Western blot

Cortical tissues were homogenized, and equal amount of proteins (30 µg) was separated on 4-12% Bis-Tris precast polyacrylamide gels by electrophoresis (200V) and transferred to nitrocellulose membranes using the Trans-Blot® Turbo TM Transfer System (Bio-Rad Laboratories, 25V for 30 min). Membranes were blocked in Odyssey blocking solution (LICOR) for 1h at room temperature and incubated overnight at 4°C with primary antibodies against UBE3A (Sigma 1404508, 1:1000), α-tubulin (Abcam ab4074, 1:5000), and actin (Sigma A3853, 1:2500). After washing in PBSTx (0.1% Triton X-100), membranes were incubated with appropriate secondary antibodies for 1 h at room temperature. Signals were detected using the Odyssey imaging system, and band intensities were quantified with Image Studio 6.0. Data were expressed as percentage relative to WT controls.

Human participants

Fifty-nine individuals with AS, recruited across multiple regions across Italy, were initially enrolled in the study. Of these, forty-nine participants (mean age = 18.35 ± 10.73 years; 24 females, 25 males) met the inclusion criteria and were retained for the analysis. Main exclusion criteria *a posteriori* were insufficient task engagement (fewer than 10 validly viewed trials) and poor signal quality, defined as ≥ 10 channels classified as invalid (“red channels”) during optode cap calibration. Forty-five age- and sex-matched neurotypical controls (mean age = 18.71± 13.13 years; 17 females, 28 males) were additionally enrolled: age matching was performed using a tolerance of ±1 year for participants aged 0–20 years and ±3 years for those aged 21–47 years. Participant demographics are summarized in Supplementary Table 3. Participation was entirely voluntary. Written informed consent was obtained from all participants or, when appropriate, from their legal guardians. All procedures were conducted in accordance with national and institutional ethical standards and complied with the principles of the World Medical Association Declaration of Helsinki (https://www.wma.net/what-we-do/medical-ethics/declaration-of-helsinki/doh-oct2008/, 1975 revised 2008). The study protocol was approved by the Regional Ethics Committee for Clinical Research of the Tuscany Region (authorization number 116/2022).

fNIRS recordings

fNIRS data acquisition was performed following the methodology described by Mazziotti et al[28]. Briefly, task-related changes in total hemoglobin (HbT) and cortical oxygenation- oxygenated (HbO) and deoxygenated hemoglobin (HbR)- were recorded from the occipital cortex using a continuous-wave system (NIRSport2, NIRx Medical Technologies). The device was equipped with eight light emitters (760 and 850 nm) and seven detectors embedded in textile caps of different sizes, yielding 22 multi-distance channels covering the visual cortical areas. To ensure consistent probe placement across participants, optodes were secured within the caps using dedicated holders and anatomical reference markers. Visual stimuli were programmed in

Python 3 using the PsychoPy3 framework[61] and presented on a 31.5-inch LG UltraGear LCD monitor (2560 × 1440 pixels, 180 Hz refresh rate; mean luminance: 400 cd/m²). Prior to data collection, the display was calibrated and gamma-corrected using a Datacolor Spyder X Pro (SXP100) colorimeter to ensure precise control of luminance and contrast.

Data were acquired using Aurora software (version 1.4.1.1) at a sampling rate of 10.2 Hz. Stimulus onset was synchronized with the NIRSport2 system via wired LAN communication using the Python implementation of LabStreamingLayer (https://github.com/sccn/labstreaminglayer), ensuring precise temporal alignment between stimulus presentation and physiological recording.

Experimental design for human study

The experimental paradigm was adapted from Mazziotti et al.[28], with minor methodological refinements. Hemodynamic responses were recorded while participants viewed their preferred video under both mock and stimulation conditions. In the mock condition, participants watched the video presented on a full-field background with uniform grey luminance, serving as baseline. In the stimulation condition, a high-contrast, black-and-white radial checkerboard with square-wave pattern reversal was superimposed to evoke visually induced hemodynamic activity[62–64]. The checkerboard stimulus (5s duration) had a spatial frequency of 0.33 cycles per degree and reversed at 4 Hz. A total of 20 trials were delivered with randomized interstimulus intervals (ISI), resulting in an overall session duration of 10 minutes. Before each recording, head circumference was measured to determine the most appropriate cap size. The cap was then positioned on the participant's head, and a calibration procedure was performed to optimize optical coupling between sources and detectors. Participants were seated 70 cm from the display monitor, and the full experimental session lasted about 20 minutes.

fNIRS data processing

To ensure robustness of the results, fNIRS data were processed using two independent preprocessing pipelines. The first pipeline (Method 1) followed the workflow described in Mazziotti et al.[28]. Briefly, raw light intensity signals were converted to optical density (OD), poor-quality channels were excluded, motion artifacts were corrected, and band-pass filtering was applied to remove physiological and instrumental noise. OD signals were then converted into concentration changes of oxygenated (ΔHbO) and deoxygenated hemoglobin (ΔHbR) using the modified Beer–Lambert law[28,65]. To enhance data reliability and minimize the influence of extreme observations, outliers were identified and excluded using the Interquartile Range (IQR) approach. For each variable, the first (Q1) and third (Q3) quartiles were computed, and the IQR was defined as Q3 − Q1. Observations falling below Q1 − 1.5 × IQR or above Q3 + 1.5 × IQR were considered outliers and excluded from subsequent analyses.

The second pipeline (Method 2) followed the same workflow but employed a more stringent, Python-based preprocessing strategy designed to mitigate motion artifacts, which are particularly prominent in individuals with AS. Full methodological details are provided in Supplementary Materials. This pipeline was developed using MNE-Python and MNE-NIRS and incorporated motion-correction procedures combining spline interpolation and wavelet filtering adapted from Homer3 into custom Python functions[66–68]. Channel quality was assessed using the Scalp Coupling Index and Peak Spectral Power, as provided by the QT-NIRS framework implemented in MNE-NIRS[69]. After conversion to hemoglobin concentrations, signals were band-pass filtered and further refined using correlation-based signal improvement (CBSI)[70]. For both pipelines, data were epoched relative to stimulus onset and baseline-corrected.

Hemodynamic responses were obtained by averaging trials within each condition over a window spanning from 1-2 s before to 20 s after stimulus onset.

To optimize signal-to-noise ratio and account for anatomical variability, two complementary strategies were applied. In Method 1, analyses focused on the "best channel", defined as the channel exhibiting the maximal peak response for each chromophore[28,29]. In Method 2, channels were ranked based on HbO response amplitude, and the top 50% were retained and averaged within each participant. This approach aimed to increase sensitivity while accounting for inter-individual variability, consistent with functionally defined channel-selection approaches in fNIRS, which improve sensitivity and can benefit from the inclusion of multiple responsive channels[71]. From these subject-level signals, key features, including area under the curve (AUC), peak amplitude, and time-to-peak, were extracted for each condition. AUC was computed using trapezoidal integration. Peak amplitude was defined as the maximum response for HbO and HbT and the minimum response for HbR, consistent with the expected polarity of the deoxygenated signal. Time to peak (TTP) was defined as the latency of this extremum and was computed for the stimulation condition only. Concentration measures are reported in mM, and integrated measures in mM·s.

The use of two independent preprocessing strategies allowed us to directly assess the robustness of the observed effects. While Method 1 reflects standard practice in the field, Method 2 provides a more conservative approach tailored to populations with increased motion and variability. The convergence of results across both pipelines strengthens confidence in the physiological validity and reproducibility of the identified hemodynamic signature.

Statistical analysis and random forest data modelling

For animal data, statistical analyses were performed using GraphPad 8.0.2. Differences between two groups were assessed using two-tailed unpaired t-tests or Mann–Whitney tests. Comparisons involving more than two groups were analyzed using one-way or two-way ANOVA followed by the Tukey multiple comparison test. Correlations between variables were evaluated using Pearson's or Spearman's correlation coefficients. Statistical results for mouse data are summarized in Supplementary Table 1.

For human data, statistical analyses were performed in a Python environment using the Pingouin statistical package, along with SciPy and Matplotlib[72–74]. Between-group effects were initially assessed using repeated-measures ANOVAs. To further characterize AS-related alterations, within-subject comparisons were subsequently conducted using post hoc tests, including Welch-corrected or paired t-tests, as appropriate. Age-related effects were assessed separately within each group using Spearman correlation. Multiple comparisons were controlled using the Benjamini–Hochberg false discovery rate (FDR) correction applied within each family of tests. To account for normative developmental effects, a smoothing spline was fitted to control data to derive an age-dependent reference curve. Individual responses from the AS group were then projected onto this model to estimate age-expected values, and deviations from these expectations were defined as age-normalized excess responses. The excess-response values were tested against zero using a one-sample directional test, and their association with age was further evaluated using directional tests on the regression slope. Additional details about age-related analyses are provided in the Supplementary Material.

Data distributions were assessed prior to analysis, and non-normally distributed data were rank-transformed where appropriate. Statistical significance was set at $p < 0.05$. Animal data are presented as mean ± SEM. For human data, representative traces are shown as mean ± SEM, while cumulative results are displayed as box plots with interquartile ranges (IQR);

individual data points correspond to single animals or participants. Statistical results for human data are summarized in Supplementary Tables 4 and 5.

To evaluate the diagnostic potential of combined imaging and behavioral readouts in the animal model, we also implemented a supervised machine learning approach. Multimodal features, including IOS-derived hemodynamic measures and behavioral performance metrics, were integrated into a unified classification framework to discriminate AS from WT mice. This approach enables a quantitative assessment of group separability and identifies the features that most strongly contribute to discrimination, providing an objective, data-driven evaluation of disease-relevant signatures with translational potential[75,76]. A Random Forest classifier (Supplementary Figure 3 and Supplementary Table 2) was selected due to its robustness in small-sample settings, its ability to handle heterogeneous multimodal features, and its reduced susceptibility to overfitting through ensemble learning[77,78]. Importantly, Random Forest models also provide intrinsic measures of feature importance, enabling interpretability and facilitating the identification of the most informative candidate biomarkers[79,80].

Acknowledgements

We are deeply grateful to Benjamin Philpot and Matt Judson for generously providing the PHP.B/hUBE3Aopt6 viral vector, which was essential for this study. We also thank Renzo Di Renzo and Elena Novelli for their valuable technical assistance. This work was supported by the Angelman Syndrome Alliance. LB also received funding from the Tuscany Health Ecosystem (THE) project (ECS_00000017), supported by the Italian Ministry of University and Research (MUR), Spoke 8. LB and RB were additionally supported by Ricerca Corrente 2025 (RC2025) from the Italian Ministry of Health.

Author Contributions

LB conceived the study and supervised the project in collaboration with IT and RB. LD, CS, GV, PJN, and LB designed the experiments and interpreted the results. LD, CS, GS, CDC, RD, FB, CB, and GP maintained the animal colony, performed the experiments, collected tissue samples, and generated the data. CS, GV and RM conducted the computational analyses. LD and LB wrote the original draft of the manuscript. All authors reviewed, revised, and approved the final manuscript.

References

1. Buiting, K., Williams, C. & Horsthemke, B. Angelman syndrome — insights into a rare neurogenetic disorder. *Nat. Rev. Neurol.* **12**, 584–593 (2016).
2. LaSalle, J. M., Reiter, L. T. & Chamberlain, S. J. Epigenetic Regulation of *UBE3A* and Roles in Human Neurodevelopmental Disorders. *Epigenomics* **7**, 1213–1228 (2015).
3. Kishino, T., Lalande, M. & Wagstaff, J. UBE3A/E6-AP mutations cause Angelman syndrome. (1997).
4. Bridges, W. A., Temples, H. S. & Lowe, T. B. Angelman Syndrome: Multidisciplinary Management. *J. Pediatr. Health Care* **39**, 968–975 (2025).
5. Milazzo, C. *et al.* Antisense oligonucleotide treatment rescues UBE3A expression and multiple phenotypes of an Angelman syndrome mouse model. *JCI Insight* **6**, e145991 (2021).
6. Judson, M. C. *et al.* Dual-isoform hUBE3A gene transfer improves behavioral and seizure outcomes in Angelman syndrome model mice. *JCI Insight* **6**, e144712 (2021).
7. Schmid, R. S. *et al.* CRISPR/Cas9 directed to the Ube3a antisense transcript improves Angelman syndrome phenotype in mice. *J. Clin. Invest.* **131**, e142574 (2021).
8. Wolter, J. M. *et al.* Cas9 gene therapy for Angelman syndrome traps Ube3a-ATS long non-coding RNA. *Nature* **587**, 281–284 (2020).
9. Li, J. *et al.* A high-fidelity RNA-targeting Cas13 restores paternal Ube3a expression and improves motor functions in Angelman syndrome mice. *Mol. Ther.* **31**, 2286–2295 (2023).
10. Vihma, H. *et al.* Ube3a unsilencer for the potential treatment of Angelman syndrome. *Nat. Commun.* **15**, 5558 (2024).
11. Meng, L. *et al.* Towards a therapy for Angelman syndrome by targeting a long non-coding RNA. *Nature* **518**, 409–412 (2015).
12. Elgersma, Y. & Sonzogni, M. UBE3A reinstatement as a disease-modifying therapy for Angelman syndrome. *Dev. Med. Child Neurol.* **63**, 802–807 (2021).
13. Jagasia, R. *et al.* Angelman syndrome patient-derived neuron screen leads to clinical ASO rugonersen targeting *UBE3A* -ATS with long-lasting effect in monkeys. *Nucleic Acids Res.* **53**, gkaf851 (2025).
14. Hipp, J. F. *et al.* The UBE3A-ATS antisense oligonucleotide rugonersen in children with Angelman syndrome: a phase 1 trial. *Nat. Med.* **31**, 2936–2945 (2025).
15. Levin, Y. *et al.* Evaluation of electroencephalography biomarkers for Angelman syndrome during overnight sleep. *Autism Res.* **15**, 1031–1042 (2022).
16. Sidorov, M. S. *et al.* Delta rhythmicity is a reliable EEG biomarker in Angelman syndrome: a parallel mouse and human analysis. *J. Neurodev. Disord.* **9**, 17 (2017).
17. Valente, K. D. *et al.* Angelman Syndrome: Difficulties in EEG Pattern Recognition and Possible Misinterpretations. *Epilepsia* **44**, 1051–1063 (2003).
18. LeBlanc, J. J. *et al.* Visual evoked potentials detect cortical processing deficits in R ett syndrome. *Ann. Neurol.* **78**, 775–786 (2015).
19. Saby, J. N. *et al.* Multisite Study of Evoked Potentials in Rett Syndrome. *Ann. Neurol.* **89**, 790–802 (2021).

20. Saby, J. N. *et al.* Electrophysiological biomarkers of brain function in CDKL5 deficiency disorder. *Brain Commun.* **4**, fcac197 (2022).
21. Mazziotti, R. *et al.* Novel translational phenotypes and biomarkers for creatine transporter deficiency. *Brain Commun.* **2**, fcaa089 (2020).
22. Du, X. *et al.* Cortical and subcortical morphological alteration in Angelman syndrome. *J. Neurodev. Disord.* **15**, 7 (2023).
23. Kim, H., Kunz, P. A., Mooney, R., Philpot, B. D. & Smith, S. L. Maternal Loss of *Ube3a* Impairs Experience-Driven Dendritic Spine Maintenance in the Developing Visual Cortex. *J. Neurosci.* **36**, 4888–4894 (2016).
24. Yashiro, K. *et al.* Ube3a is required for experience-dependent maturation of the neocortex. *Nat. Neurosci.* **12**, 777–783 (2009).
25. Sonzogni, M. *et al.* A behavioral test battery for mouse models of Angelman syndrome: a powerful tool for testing drugs and novel Ube3a mutants. *Mol. Autism* **9**, 47 (2018).
26. Lee, D. *et al.* Antisense oligonucleotide therapy rescues disturbed brain rhythms and sleep in juvenile and adult mouse models of Angelman syndrome. *eLife* **12**, e81892 (2023).
27. Spencer, E. R. *et al.* Longitudinal EEG model detects antisense oligonucleotide treatment effect and increased UBE3A in Angelman syndrome. *Brain Commun.* **4**, fcac106 (2022).
28. Mazziotti, R. *et al.* The amplitude of fNIRS hemodynamic response in the visual cortex unmasks autistic traits in typically developing children. *Transl. Psychiatry* **12**, 53 (2022).
29. Scaffei, E. *et al.* A Potential Biomarker of Brain Activity in Autism Spectrum Disorders: A Pilot fNIRS Study in Female Preschoolers. *Brain Sci.* **13**, 951 (2023).
30. Ward, L. M., Aitchison, R. T., Tawse, M., Simmers, A. J. & Shahani, U. Reduced Haemodynamic Response in the Ageing Visual Cortex Measured by Absolute fNIRS. *PloS One* **10**, e0125012 (2015).
31. West, K. L. *et al.* BOLD hemodynamic response function changes significantly with healthy aging. *NeuroImage* **188**, 198–207 (2019).
32. Niehaus, L., Lehmann, R., Röricht, S. & Meyer, B. U. Age-related reduction in visually evoked cerebral blood flow responses. *Neurobiol. Aging* **22**, 35–38 (2001).
33. Sun, J., Liu, Y., Hao, X., Baudry, M. & Bi, X. Lack of UBE3A-Mediated Regulation of Synaptic SK2 Channels Contributes to Learning and Memory Impairment in the Female Mouse Model of Angelman Syndrome. *Neural Plast.* **2022**, 1–9 (2022).
34. Huang, H.-S. *et al.* Behavioral deficits in an Angelman syndrome model: Effects of genetic background and age. *Behav. Brain Res.* **243**, 79–90 (2013).
35. Santini, E. *et al.* Mitochondrial Superoxide Contributes to Hippocampal Synaptic Dysfunction and Memory Deficits in Angelman Syndrome Model Mice. *J. Neurosci.* **35**, 16213–16220 (2015).
36. Su, H. *et al.* Mitochondrial dysfunction in CA1 hippocampal neurons of the UBE3A deficient mouse model for Angelman syndrome. *Neurosci. Lett.* **487**, 129–133 (2011).

37. Aria, F., Pandey, K. & Alberini, C. M. Excessive Protein Accumulation and Impaired Autophagy in the Hippocampus of Angelman Syndrome Modeled in Mice. *Biol. Psychiatry* **94**, 68–83 (2023).
38. Simchi, L., Gupta, P. K., Feuermann, Y. & Kaphzan, H. Elevated ROS levels during the early development of Angelman syndrome alter the apoptotic capacity of the developing neural precursor cells. *Mol. Psychiatry* **28**, 2382–2397 (2023).
39. Gupta, P. K., Barak, S., Feuermann, Y., Goobes, G. & Kaphzan, H. 1H-NMR-based metabolomics reveals metabolic alterations in early development of a mouse model of Angelman syndrome. *Mol. Autism* **15**, 31 (2024).
40. Rotaru, D. C., Mientjes, E. J. & Elgersma, Y. Angelman Syndrome: From Mouse Models to Therapy. *Neuroscience* **445**, 172–189 (2020).
41. Sidorov, M. S. *et al.* Enhanced Operant Extinction and Prefrontal Excitability in a Mouse Model of Angelman Syndrome. *J. Neurosci.* **38**, 2671–2682 (2018).
42. Kaphzan, H., Buffington, S. A., Jung, J. I., Rasband, M. N. & Klann, E. Alterations in Intrinsic Membrane Properties and the Axon Initial Segment in a Mouse Model of Angelman Syndrome. *J. Neurosci.* **31**, 17637–17648 (2011).
43. Kaphzan, H. *et al.* Genetic Reduction of the α1 Subunit of Na/K-ATPase Corrects Multiple Hippocampal Phenotypes in Angelman Syndrome. *Cell Rep.* **4**, 405–412 (2013).
44. Townsend, L. B., Jones, K. A., Dorsett, C. R., Philpot, B. D. & Smith, S. L. Deficits in higher visual area representations in a mouse model of Angelman syndrome. *J. Neurodev. Disord.* **12**, 28 (2020).
45. Judson, M. C. *et al.* GABAergic Neuron-Specific Loss of Ube3a Causes Angelman Syndrome-Like EEG Abnormalities and Enhances Seizure Susceptibility. *Neuron* **90**, 56–69 (2016).
46. Wallace, M. L., Burette, A. C., Weinberg, R. J. & Philpot, B. D. Maternal Loss of Ube3a Produces an Excitatory/Inhibitory Imbalance through Neuron Type-Specific Synaptic Defects. *Neuron* **74**, 793–800 (2012).
47. Wallace, M. L., Van Woerden, G. M., Elgersma, Y., Smith, S. L. & Philpot, B. D. *Ube3a* loss increases excitability and blunts orientation tuning in the visual cortex of Angelman syndrome model mice. *J. Neurophysiol.* **118**, 634–646 (2017).
48. Theparambil, S. M. *et al.* Adenosine signalling to astrocytes coordinates brain metabolism and function. *Nature* **632**, 139–146 (2024).
49. Moreira-de-Sá, A. *et al.* Adenosine A2A receptors format long-term depression and memory strategies in a mouse model of Angelman syndrome. *Neurobiol. Dis.* **146**, 105137 (2020).
50. Moreira-de-Sá, A. *et al.* Motor Deficits Coupled to Cerebellar and Striatal Alterations in Ube3am−/p+ Mice Modelling Angelman Syndrome Are Attenuated by Adenosine A2A Receptor Blockade. *Mol. Neurobiol.* **58**, 2543–2557 (2021).
51. Hagenaar, D. A. *et al.* Outcome measures in Angelman syndrome. *J. Neurodev. Disord.* **16**, 6 (2024).

52. Walz, N. C. & Baranek, G. T. Sensory processing patterns in persons with Angelman syndrome. *Am. J. Occup. Ther. Off. Publ. Am. Occup. Ther. Assoc.* **60**, 472–479 (2006).
53. Neklyudova, A., Smirnov, K., Rebreikina, A., Martynova, O. & Sysoeva, O. Electrophysiological and Behavioral Evidence for Hyper- and Hyposensitivity in Rare Genetic Syndromes Associated with Autism. *Genes* **13**, 671 (2022).
54. Hong, M. P. *et al.* Eye gaze and pupillary response in Angelman syndrome. *Res. Dev. Disabil.* **68**, 88–94 (2017).
55. Heald, M., Adams, D. & Oliver, C. Profiles of atypical sensory processing in Angelman, Cornelia de Lange and Fragile X syndromes. *J. Intellect. Disabil. Res. JIDR* **64**, 117–130 (2020).
56. Jiang, Y. *et al.* Mutation of the Angelman Ubiquitin Ligase in Mice Causes Increased Cytoplasmic p53 and Deficits of Contextual Learning and Long-Term Potentiation. *Neuron* **21**, 799–811 (1998).
57. Lee, H.-M. *et al.* Characterization and structure-activity relationships of indenoisoquinoline-derived topoisomerase I inhibitors in unsilencing the dormant Ube3a gene associated with Angelman syndrome. *Mol. Autism* **9**, 45 (2018).
58. Mazziotti, R. *et al.* Searching for biomarkers of CDKL5 disorder: early-onset visual impairment in CDKL5 mutant mice. *Hum. Mol. Genet.* **26**, 2290–2298 (2017).
59. Lupori, L. *et al.* Site-specific abnormalities in the visual system of a mouse model of CDKL5 deficiency disorder. *Hum. Mol. Genet.* **28**, 2851–2861 (2019).
60. Swayze, E. E. *et al.* Antisense oligonucleotides containing locked nucleic acid improve potency but cause significant hepatotoxicity in animals. *Nucleic Acids Res.* **35**, 687–700 (2007).
61. Peirce, J. *et al.* PsychoPy2: Experiments in behavior made easy. *Behav. Res. Methods* **51**, 195–203 (2019).
62. Wijeakumar, S., Shahani, U., Simpson, W. A. & McCulloch, D. L. Localization of Hemodynamic Responses to Simple Visual Stimulation: An fNIRS Study. *Investig. Opthalmology Vis. Sci.* **53**, 2266 (2012).
63. Pinti, P. *et al.* The present and future use of functional near-infrared spectroscopy (fNIRS) for cognitive neuroscience. *Ann. N. Y. Acad. Sci.* **1464**, 5–29 (2020).
64. Chen, L.-C., Sandmann, P., Thorne, J. D., Herrmann, C. S. & Debener, S. Association of Concurrent fNIRS and EEG Signatures in Response to Auditory and Visual Stimuli. *Brain Topogr.* **28**, 710–725 (2015).
65. Di Lorenzo, R. *et al.* Recommendations for motion correction of infant fNIRS data applicable to multiple data sets and acquisition systems. *NeuroImage* **200**, 511–527 (2019).
66. Gramfort, A. *et al.* MEG and EEG data analysis with MNE-Python. *Front. Neurosci.* **7**, 267 (2013).
67. Luke, R. *et al.* Analysis methods for measuring passive auditory fNIRS responses generated by a block-design paradigm. *Neurophotonics* **8**, 025008 (2021).

68. Huppert, T. J., Diamond, S. G., Franceschini, M. A. & Boas, D. A. HomER: a review of time-series analysis methods for near-infrared spectroscopy of the brain. *Appl. Opt.* **48**, D280-298 (2009).
69. Hernandez, S. M. & Pollonini, L. NIRSplot: A Tool for Quality Assessment of fNIRS Scans. in *Biophotonics Congress: Biomedical Optics 2020 (Translational, Microscopy, OCT, OTS, BRAIN)* BM2C.5 (Optica Publishing Group, Washington, DC, 2020). doi:10.1364/BRAIN.2020.BM2C.5.
70. Cui, X., Bray, S. & Reiss, A. L. Functional near infrared spectroscopy (NIRS) signal improvement based on negative correlation between oxygenated and deoxygenated hemoglobin dynamics. *NeuroImage* **49**, 3039–3046 (2010).
71. Liu, Y., Sánchez Hernández, F., Ting, F. & Hyde, D. C. Comparing fixed-array and functionally-defined channel of interest approaches to infant functional near-infrared spectroscopy data. *NeuroImage* **261**, 119520 (2022).
72. Gollapudi, S. OpenCV with Python. in *Learn Computer Vision Using OpenCV* 31–50 (Apress, Berkeley, CA, 2019). doi:10.1007/978-1-4842-4261-2_2.
73. Vallat, R. Pingouin: statistics in Python. *J. Open Source Softw.* **3**, 1026 (2018).
74. Hunter, J. D. Matplotlib: A 2D Graphics Environment. *Comput. Sci. Eng.* **9**, 90–95 (2007).
75. Orrù, G., Pettersson-Yeo, W., Marquand, A. F., Sartori, G. & Mechelli, A. Using Support Vector Machine to identify imaging biomarkers of neurological and psychiatric disease: A critical review. *Neurosci. Biobehav. Rev.* **36**, 1140–1152 (2012).
76. Woo, C.-W., Chang, L. J., Lindquist, M. A. & Wager, T. D. Building better biomarkers: brain models in translational neuroimaging. *Nat. Neurosci.* **20**, 365–377 (2017).
77. Breiman, L. Random Forests. *Mach. Learn.* **45**, 5–32 (2001).
78. Biau, G. & Scornet, E. A random forest guided tour. *TEST* **25**, 197–227 (2016).
79. Topol, E. J. High-performance medicine: the convergence of human and artificial intelligence. *Nat. Med.* **25**, 44–56 (2019).
80. Beam, A. L. & Kohane, I. S. Big Data and Machine Learning in Health Care. *JAMA* **319**, 1317 (2018).

Figures

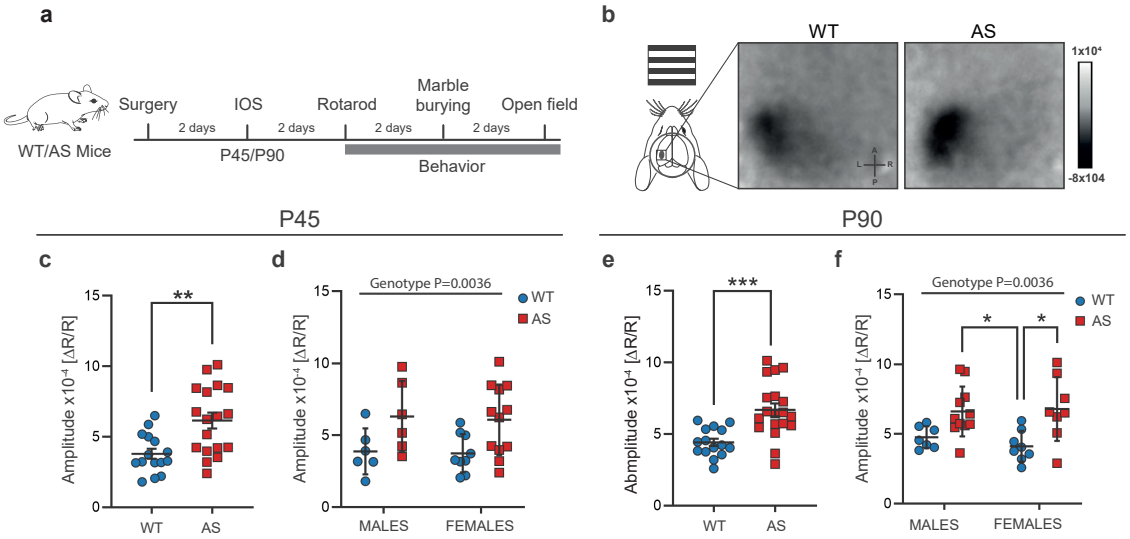


Figure 1. Visually evoked hemodynamic responses in WT and AS mice. (a) Experimental design to assess visual IOS responses in WT and AS animals. (b) Representative IOS cortical response elicited by contralateral eye stimulation in WT and AS mice. LUT is shown on the right. (c, d) Quantification of IOS responses in juvenile mice (P45). IOS amplitude is shown across genotypes (c) and separated by sex within each genotype (d). (e, f) Quantification of IOS responses in adult mice (P90). IOS amplitude is shown across genotypes (e) and separated by sex within each genotype (f). WT animals are shown as blue circles, while AS mice are shown as red squares. Statistical details are reported in Supplementary Table 1. *p < 0.05, **p<0.01.

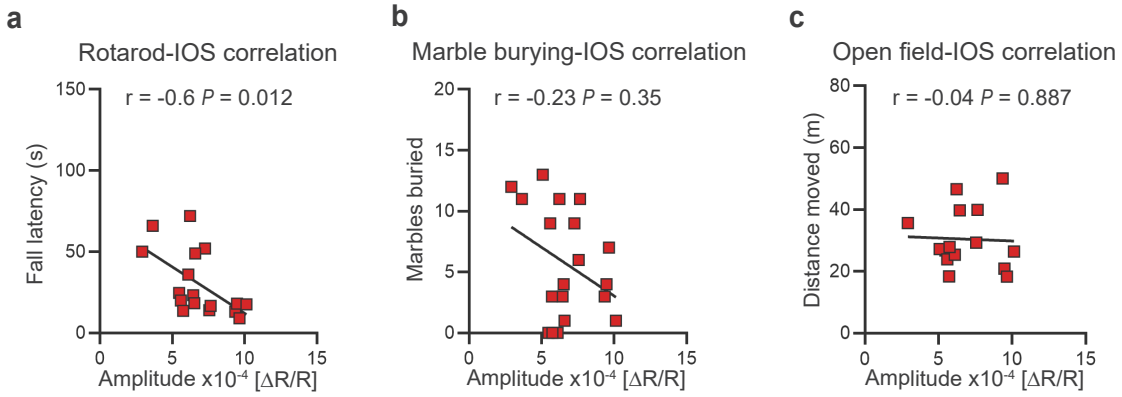


Figure 2. Correlation between IOS responses and behavioral performance in adult AS mice. Relationship between IOS responses and behavioral performance in the rotarod (a), marble burying (b), and open field (c) in AS mice. Statistical details are reported in Supplementary Table 1.

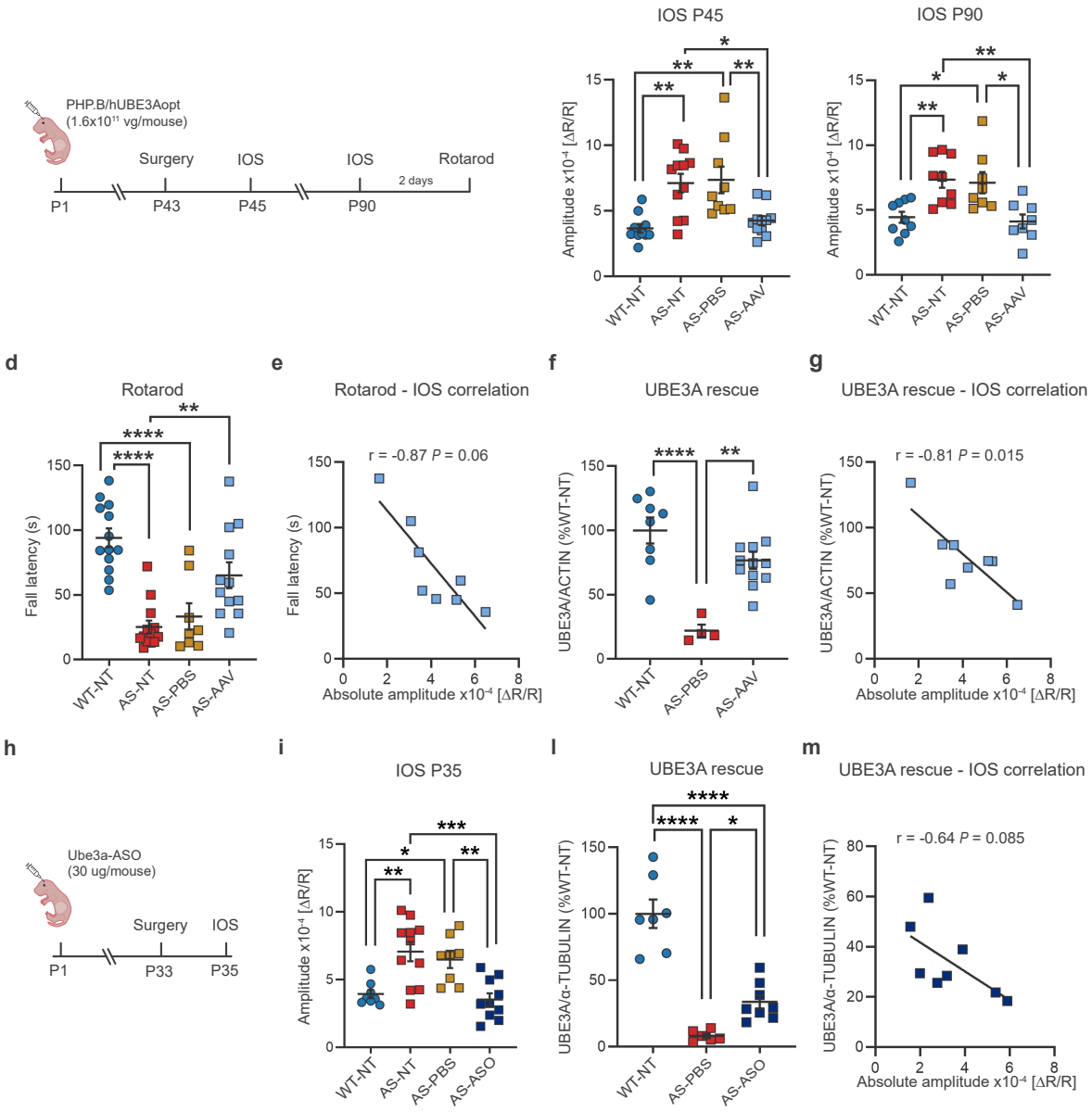


Figure 3. Visually evoked IOS responses to therapeutic intervention in AS mice. (a) Experimental design used to assess biomarker responsiveness to gene transfer therapy. (b, c) Visual IOS amplitude in non-treated (WT-NT and AS-NT), AS-PBS, and AS-AAV juvenile (b) and adult (c) mice. (d) Rotarod latency to fall in adult animals. (e) Correlation between IOS responses and rotarod performance in AS-AAV mice. (f) Western blot of cortical lysates obtained from WT-NT, AS-PBS, and AS-AAV mice. (g) Correlation between IOS responses and cortical UBE3A protein levels in AS-AAV mice. (h) Experimental design used to assess biomarker responsiveness to ASO therapy. (i) Visual IOS amplitude in untreated (WT-NT and AS-NT), AS-PBS, and AS-ASO mice at P35. (l) Western blot of cortical lysates obtained from WT-NT, AS-PBS, and AS-ASO mice. (m) Correlation between IOS responses and UBE3A protein level in AS-ASO mice. Statistical details are reported in Supplementary Table 1. *p< 0.05, **p< 0.01, ***p< 0.001, ****p< 0.0001. WT-NT, blue circles; AS-NT, red squares; AS-PBS, yellow squares; AS-AAV, light blue squares; AS-ASO, dark blue squares.

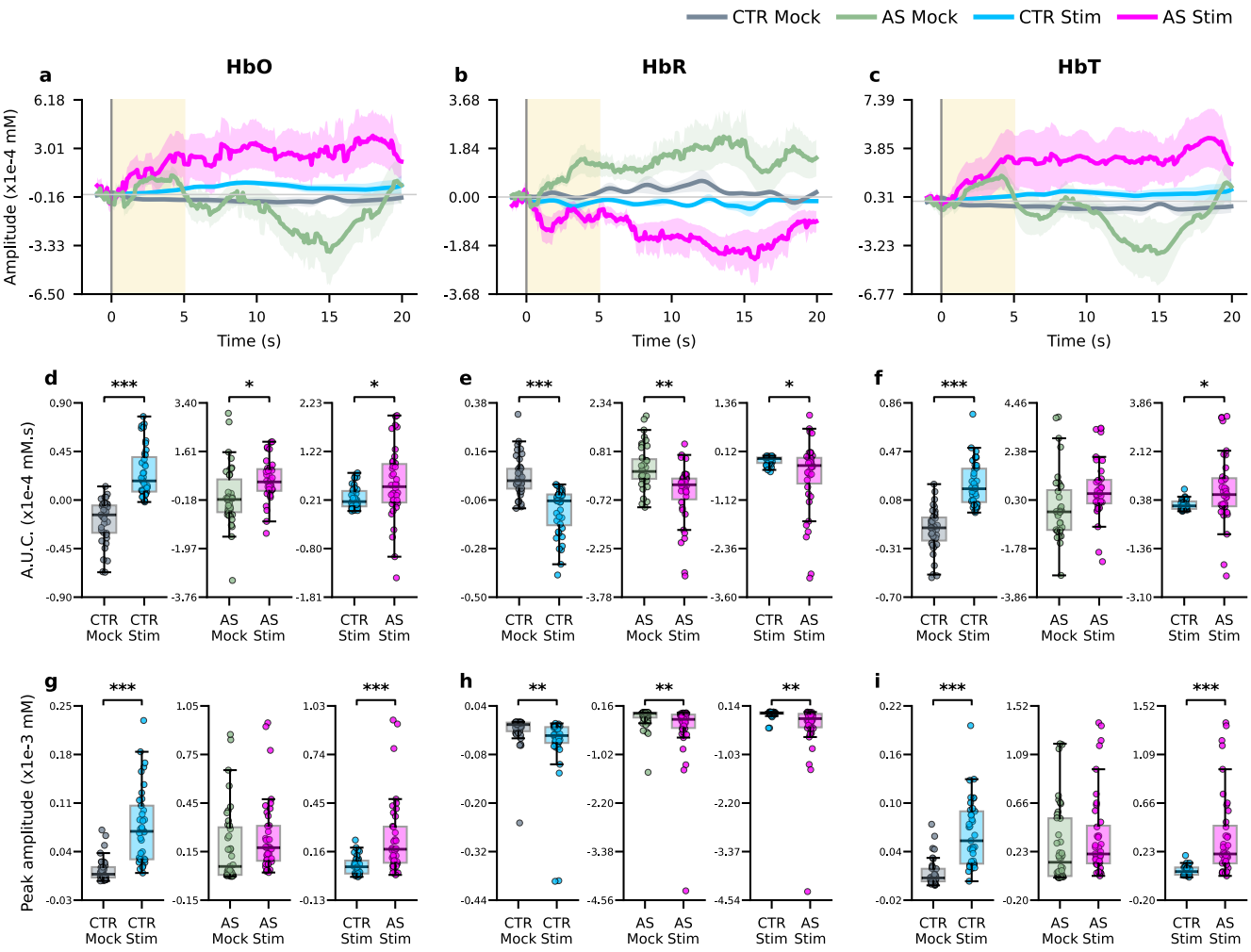


Figure 4. Visually evoked hemodynamic responses in control participants and individuals with AS (preprocessing method 1). (a-c) Grand-average time courses of oxygenated (HbO), deoxygenated (HbR), and total hemoglobin (HbT) during visual stimulation and mock condition. Traces are shown as mean ± SEM across participants. Control participants (CTR) are shown in gray (mock) and blue (stimulation), while individuals with Angelman syndrome (AS) are shown in green (mock) and magenta (stimulation). Time 0 indicates stimulus onset; the shaded yellow window denotes the stimulation period. (d-f) Quantification of the area under the curve (AUC) for HbO, HbR, and HbT across conditions and groups. Boxplots show the distribution of individual participant values (center line: median; box: interquartile range; whiskers: range). (g-i) Peak amplitude of the hemodynamic response for HbO, HbR, and HbT across conditions and groups, defined as the maximum change from baseline within the post-stimulus window. Statistical details are reported in Supplementary Table 4-5. *p < 0.05, **p < 0.01, ***p < 0.001.

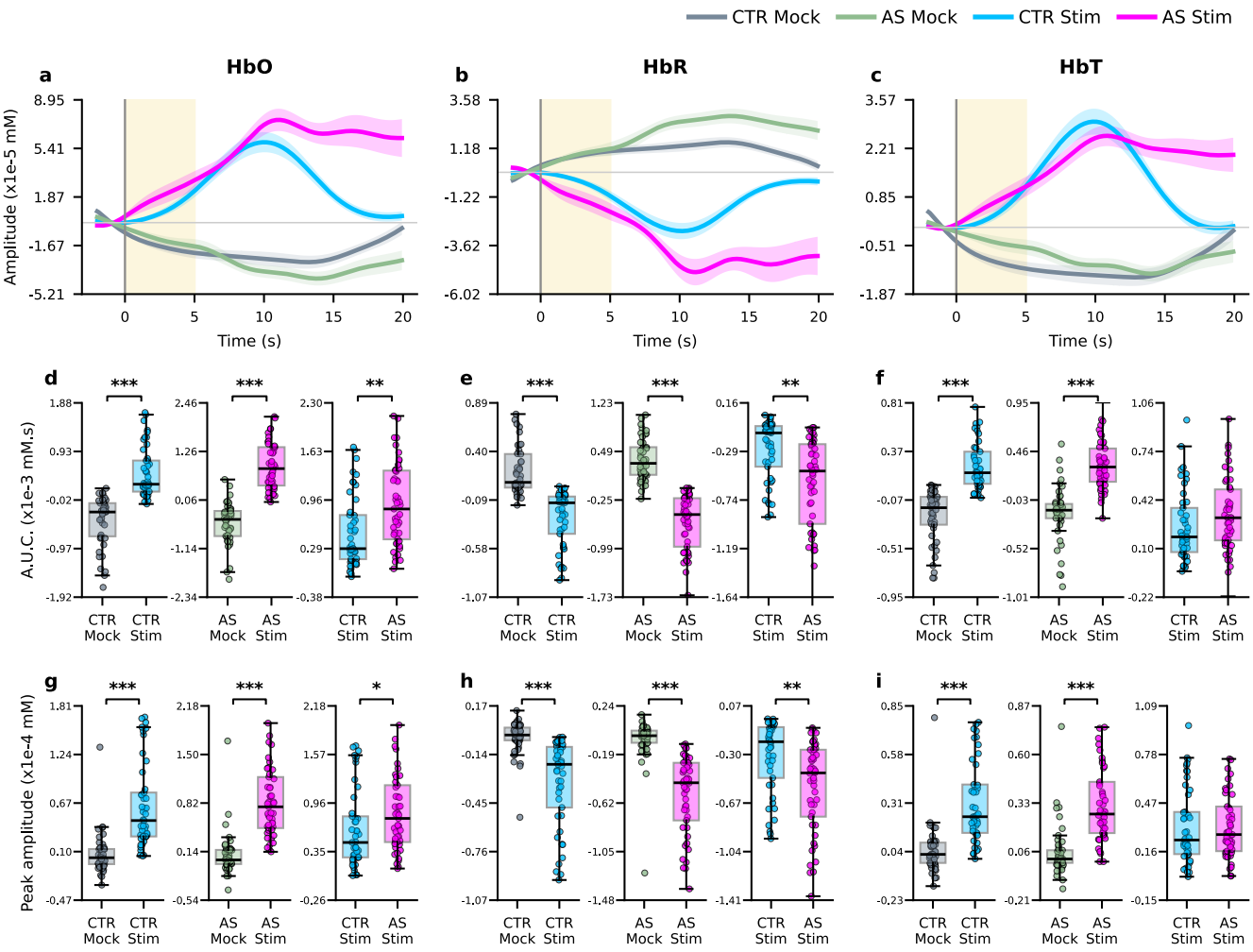


Figure 5. Visually evoked hemodynamic responses in control participants and individuals with AS (preprocessing pipeline 2). (a-c) Grand-average time courses of oxygenated (HbO), deoxygenated (HbR), and total hemoglobin (HbT) during visual stimulation and mock condition. Traces are shown as mean ± SEM across participants. Control participants (CTR) are shown in gray (mock) and blue (stimulation), while individuals with Angelman syndrome (AS) are shown in green (mock) and magenta (stimulation). Time 0 indicates stimulus onset; the shaded yellow window denotes the stimulation period. (d-f) Quantification of the area under the curve (AUC) for HbO, HbR, and HbT across conditions and groups. Boxplots show the distribution of individual participant values (center line: median; box: interquartile range; whiskers: range). (g-i) Peak amplitude of the hemodynamic response for HbO, HbR, and HbT across conditions and groups, defined as the maximum change from baseline within the post-stimulus window. Statistical details are reported in Supplementary Table 4-5. *p < 0.05, **p < 0.01, ***p < 0.001.

Supplementary Files

This is a list of supplementary files associated with this preprint. Click to download.

- DadXXetal.Supplementarymaterial.pdf